INFORMATICS JOURNALS

ISSN (Print) : 0013-466X
ISSN (Online) : xxxx-xxxx

The Journal of Electrochemical Society of India, Volume 75, Issue (2), April-June 2026; pp. 106-125

DOI: 10.18311/JESCI/2026/39363

Microstructural, Mechanical and Corrosion Assessment of Ti-Cu Alloys Prepared by Molten Salt Electro-Deoxidation Process

Haritha Rajasekaran[1], Anwesha Mukherjee[1#], Swetha Muraleedharan[1,2], S. Maharajan[1] and R. Kumaresan[1,2*]

[1]Indira Gandhi Centre for Atomic Research, DAE Township, Kalpakkam, Chengalpattu District - 603102, Tamil Nadu, India

[2]Homi Bhabha National Institute, Training School Complex, Anushaktinagar - 400094, Mumbai, India

Abstract

Titanium-copper alloys with compositions Ti-2.5Cu, Ti-5Cu, and Ti-10Cu were produced from sintered mixed oxides of TiO_2 and CuO, via direct oxide electro-reduction using the Fray-Farthing-Chen (FFC) Cambridge process in molten $CaCl_2$ at 850 °C. The electro-deoxidation experiments were performed over various time intervals at a cell voltage of 3.1 V between the sintered mixed-oxide cathode and the graphite anode. The reduced products were characterized using X-ray diffraction, scanning electron microscopy, and energy-dispersive X-ray spectroscopy techniques to determine the reduction mechanism of the metal oxide mixture. XRD patterns indicated that the Ti-Cu alloys were composed of α-Ti and Ti_2Cu phases. The presence of the Ti_2Cu phase became more significant with increasing Cu content in the alloy. Mechanical testing showed an increase in elastic modulus and Vickers hardness as Cu content increased. The corrosion behavior of the alloys was evaluated in 3.5 wt.% NaCl solution at 25°C for 24 h. Potentiodynamic polarization and Electrochemical Impedance Spectroscopy (EIS) studies demonstrated the passivation behavior of the alloys and showed the best corrosion resistance at 5 wt.% Cu concentration.

Keywords: Corrosion, Cyclic Voltammetry, Elastic Modulus, Electro-Deoxidation, Molten Salts, Ti-Cu Alloys, Vickers Hardness

1. Introduction

Titanium and its alloys exhibit a combination of excellent properties, including a high strength-to-weight ratio, outstanding corrosion resistance, and remarkable biocompatibility[1-3]. Titanium alloys are in high demand for a wide range of applications across various industries, including aeronautics, the biomedical sector, nuclear energy, and the marine industry. Titanium alloy (Grade II) has been used commercially in marine applications. However, its exposure to the seawater environment within the heat exchangers results in ruptures due to hydrogen-assisted corrosion[4]. The failure of a Ti condenser tube in a seawater environment due to the erosion-corrosion caused by the turbulent flow in the biofouling area has been reported[5]. Therefore, it is crucial to improve their biocompatibility and anti-corrosion performance in marine environments[6,7].

Copper has unique properties, including malleability, biocompatibility, antimicrobial activity,

*Author for correspondence
#2nd Author for correspondence

*Email: rkum@igcar.gov.in, anwesha@igcar.gov.in

and corrosion resistance. It has a wide range of applications across various industries[8,9]. Copper also serves as an active eutectoid β stabilizer in titanium alloys and effectively lowers the melting temperature of Ti-Cu alloys. Titanium-rich copper alloys are composed of α-Ti and Ti_2Cu phases, where the corrosion performance is influenced by the distribution and quantity of Ti_2Cu[10,11]. While an over-the-top copper content may promote Cu-rich intermetallic phases and adversely affect corrosion resistance, controlled Cu additions can enhance the mechanical and functional characteristics of Ti alloys[12-14].

Ti-Cu alloys have been well researched and optimized for their antibacterial activity, mechanical performance and corrosion resistance; however, their resulting properties are strongly influenced by the preparation technique employed. Preparation methods such as casting[15], powder metallurgy[15], semi-solid metal processing[15], additive manufacturing[15,16], and selective laser melting[17] were adopted by the researchers to prepare Ti–Cu alloys with control over microstructure and properties. These traditional routes generally involve melting, powder consolidation, or localized melting and are therefore strongly influenced by solidification, segregation, non-uniform microstructures, a lack of control over alloy oxidation, processing conditions, and the requirement of post-processing[15-20]. Moreover, a few of these processes lack scalability, are cost-intensive, and are yet to be developed for industry[15]. On the other hand, the Fray-Farthing-Chen (FFC) Cambridge process is a solid-state electrochemical technique in which metal oxides can be directly reduced to porous metallic structures using electrons as the reductant in a molten salt medium (electroreduction/deoxidation), thereby eliminating the need for a conventional melting step. It has been extensively used for producing porous metals and alloys[21]. The process has demonstrated lower energy consumption and processing steps than the conventional alloying processes. During this process, constant-voltage electrolysis is performed in molten $CaCl_2$ at high temperature (800-900 °C) between a solid, porous oxide cathode and a graphite anode, enabling single-step conversion of oxides to metals and alloys. In this method, the simultaneous elimination of oxygen generates interconnected porosity, which is ideal for energy-related devices, biomedical implants, and catalytic systems[22,23]. Recent literature highlighted its application for synthesizing a diverse range of metallic systems, including more reactive metals such as Titanium (Ti), Zirconium (Zr), Chromium (Cr), Niobium (Nb), Tantalum (Ta), Silicon (Si), and Uranium (U), as well as Ti-based binary and ternary alloys[24,25]. However, the electro-deoxidation pathway and the evolution of the Ti_2Cu phase during the direct synthesis of Ti–Cu alloys from TiO_2–CuO mixed oxides in molten $CaCl_2$, and their relationship to the final microstructure, mechanical properties, and corrosion characteristics, have not been thoroughly studied.

In this present study, Ti-xCu alloys with different copper contents (x=2.5, 5 and 10 wt. %) were prepared from their respective oxide mixtures using molten $CaCl_2$ as the electrolyte medium *via* the FFC Cambridge process. The mechanism of formation of these alloys from their respective oxides is systematically investigated. In addition, the effects of Cu content on the microstructure, mechanical properties, and corrosion resistance (in 3.5 wt.% NaCl solution) were also discussed. The Cu content used in this study was limited to 10 wt.% because, beyond this threshold, excessive intermetallics destabilize the microstructure and reduce corrosion resistance[26]. The unique contribution of this work is to establish the connection between the FFC electro-deoxidation route and the evolution of the Ti_2Cu phase, and to correlate these with the microstructure, mechanical properties, and corrosion behavior of Ti–Cu alloys.

2. Experimental

2.1 Preparation of Anhydrous $CaCl_2$, Metal Oxide Preforms and Electrodes

Calcium chloride dihydrate ($CaCl_2{\cdot}2H_2O$), obtained commercially from Merck (ACS grade, minimum

purity of 99%), was used to prepare the calcium chloride melt. It was prepared following methodologies previously reported in the literature[27]. Commercially available powders of rutile TiO_2 (Thermo Scientific, 99.99% purity, metals basis) and CuO (GR grade, 99 % purity, metals basis) were weighed in the required proportions to achieve final alloy compositions of Ti-2.5Cu, Ti-5Cu, and Ti-10 Cu (values in wt.%). The powders were blended with 1 wt.% Polyvinyl Alcohol (PVA) solution and 0.5 wt.% Polyethylene Glycol (PEG) solution. The mixture was dried under an IR lamp and subsequently ground using agate balls in a ball mill (M/s LABINDIA Planetary Ball Mill, BM1150+) for 3 hours at 300 rpm. The powders were uniaxially pressed into discs, each weighing 1 g and having a diameter of 12.5 mm, and then sintered in air at 900 °C for 4 h using a Carbolite RHF 1600 furnace. The open porosity of the sintered mixed oxide pellets was determined using the water impregnation method based on Archimedes' principle.

The electrodes used in the molten salt experiments included High-Density (HD) graphite rods (10 mm diameter, 100 mm length, density 1.85 g/cc, M/s Nikunj Group, Mumbai, India), tungsten wire (1 mm diameter, Thermo Scientific, 99.95 % purity, metals basis), molybdenum coil (Thermo Scientific, 99.94 % purity, metals basis), sintered mixed oxide pellets, oxide powder-filled Metallic Cavity Electrode (MCE), and Ni|NiO reference electrode. Metallic Cavity Electrodes (MCEs) measuring 60 mm in length, 3 mm in breadth, and 0.25 mm in thickness were fabricated using molybdenum foil (Thermo Scientific, 99.95 % purity, metals basis, 0.25 mm thickness). The preparation of Ni|NiO reference electrodes and MCEs has been described in earlier studies[28,29]. A sintered mixed oxide pellet was fixed in a cradle prepared from tantalum wire (Thermo Scientific, 99.95 % purity, metals basis, 1 mm diameter) and was tied with tantalum wire of 0.5 mm diameter in order to raise the contact points between metal and mixed oxide. All electrodes were connected to Stainless Steel (SS) rods (1.6 mm diameter), which served as current leads. To ensure electrical insulation, the current leads were encased in alumina sleeves.

2.2 Electrochemical Setup and Procedure

Cyclic Voltammetry (CV) and electro-deoxidation experiments were performed using a molten salt electrolysis cell, by methodologies detailed in the literature[30]. A crucible made of SS 316L containing approximately 300 g of vacuum-dried $CaCl_2$ was placed in the lower compartment of an Inconel 600 electrochemical cell. The cell was assembled in a high-purity argon glove box to maintain an inert atmosphere suitable for cyclic voltammetry and electro-deoxidation analyses. The electrochemical cell was heated to 850 °C within a vertical pit-type furnace and continuously maintained under an inert atmosphere via the dynamic flow of high-purity argon gas. After approximately one hour of thermal equilibration, pre-electrolysis was performed to remove electrochemically active impurities. This was achieved by maintaining a constant potential of 2.8 V applied across a Mo coil cathode and a graphite rod anode, until the current reached a minimal steady-state level.

Cyclic voltammetry of molten $CaCl_2$ was carried out by using W (cathodic polarization) and HD graphite rod (anodic polarization) as working electrodes, while the Mo wire and HD graphite rod served as the counter electrodes for the cathodic and anodic configurations at 850 °C. Electro-deoxidation of the mixed oxides was subsequently carried out by applying a constant potential of 3.1 V for different durations between a sintered metal oxide disc (cathode) and a graphite rod (anode) *via* a DC power supply unit (KEYSIGHT TECHNOLOGIES, E3633A). The electrodes were raised above the melt once the electro-deoxidation process was finished, and the cell was left to cool to room temperature. After allowing the cell to reach room temperature, it was moved to the argon glove box for the recovery of the electrolyzed product. The reduced product was thoroughly cleaned with water to remove any remaining salt, and then vacuum-dried. The XRD of the precursor oxide pellets and the processed alloy

samples (uniformly ground powder) were recorded using M/s GNR Explorer, Italy, with Cu K-α radiation (λ = 1.5416 Å). The cross-sectional morphology and elemental composition were examined using SEM (ZEISS Crossbeam 340, Germany) equipped with an EDS attachment. Gold sputter coating was applied to the sintered oxide pellets prior to SEM analysis to mitigate charging effects.

2.3 Mechanical Properties and Corrosion Behavior

The mechanical properties of the alloys were evaluated through measurements of elastic modulus and Vickers hardness. For hardness testing, the alloy samples were sectioned, hot-mounted in resin, and polished using a SiC abrasive paper up to 1500 grit. Then, it was measured using a Vickers hardness tester (MHT3, Anton Paar) by applying a load of 1 N for a dwell time of 15 s, and the indentations were imaged with a metallurgical optical microscope. To determine the elastic modulus, alloy specimens were machined into rectangular bars and tested using a 4-point bending setup. For every sample, at least three indentations were made, and the average values were reported. The open porosity of the electro-reduced alloys was measured using the water impregnation method based on Archimedes' principle.

The corrosion properties of the alloys prepared were evaluated in 3.5 wt.% NaCl solution at room temperature. The electro-reduced alloy was used as the working electrode in the electrochemical cell, with Ag/AgCl and a Pt coil serving as the reference and counter electrodes, respectively. The alloys were immersed in the NaCl solution for 24 hours and subjected to potentiodynamic polarization and electrochemical impedance spectroscopy studies. All of these electrochemical measurements were carried out with the help of METROHM AUTOLAB PGSTAT 302N potentiostat/galvanostat and the data were recorded and analyzed using NOVA 2.1.9 software. The polarization studies were performed in the potential range −0.5 to +2 V vs Ag/AgCl at a scan rate of 1 mV s^{-1}. The EIS studies were carried out at open-circuit potentials using a perturbation signal with an a.c. amplitude of ±10 mV in the frequency range of 0.1 Hz to 5000 Hz at 10 cycles per decade.

3. Results and Discussion

3.1 Characterization of Sintered Metal Oxide Precursors

The open porosity of the sintered pellets was determined to be in the range 35.7-37.9%. The XRD patterns of the sintered pellets are shown in Figure 1. All samples contained TiO_2 and CuO with crystal systems tetragonal and monoclinic, respectively. The intensity of the CuO peaks increased with increasing CuO content. The elemental composition of all the sintered mixed oxide pellets, as determined from their EDS map sum spectrum, consisted of Ti (52.8-59.4 wt.%), Cu (1.6-6.2 wt.%), and O (36.7-43.4 wt.%), respectively.

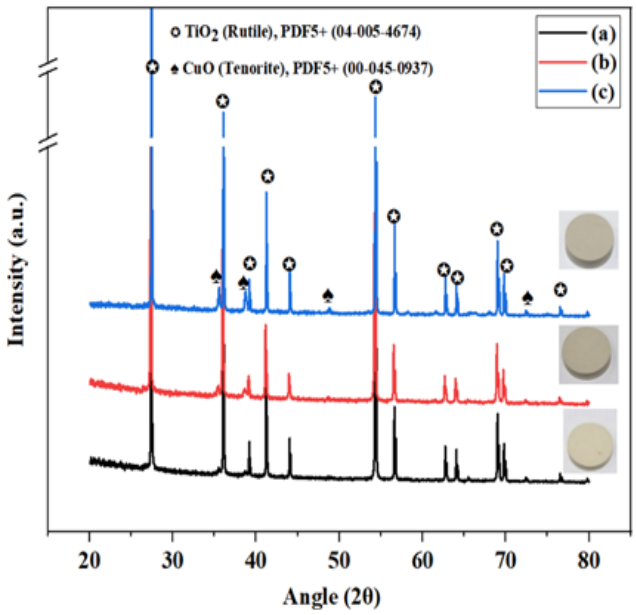


Figure 1. XRD patterns of TiO_2-CuO mixed oxide pellets, sintered at 900 °C in air for 4 h, corresponding to the alloy compositions of **(a)** Ti-2.5Cu, **(b)** Ti-5Cu, and **(c)** Ti-10Cu. Insets show photographs of the pellets.

3.2 Cyclic Voltammetry Studies on Mixed Oxide Precursor

The cyclic voltammograms with and without oxide powder-filled MCE were rescaled against the $Ca^{2+}|Ca$ potential (-2.297 V vs Ni|NiO) for better comparison. Figure 2 displays the cyclic voltammograms of a blank Metal Cavity Electrode (MCE) and a TiO_2-CuO (corresponding to a Ti-10Cu alloy) powder-filled MCE in a $CaCl_2$ melt at 850 °C. The mixed oxide MCE CVs exhibited four reduction peaks at 1.843 V (C_1), 1.477 V (C_2), 1.179 V (C_3) and 0.458 V (C_4) prior to the calcium deposition potential. Multiple oxidation peaks were observed in the anodic scan, indicating that different Ti-O phases formed during the reoxidation of Ti. Under inert conditions, CuO is less stable at high temperature and easily gets converted to Cu_2O[31,32]. Therefore, the initial reduction peak, C_1 can be attributed to the reduction of Cu_2O to Cu.

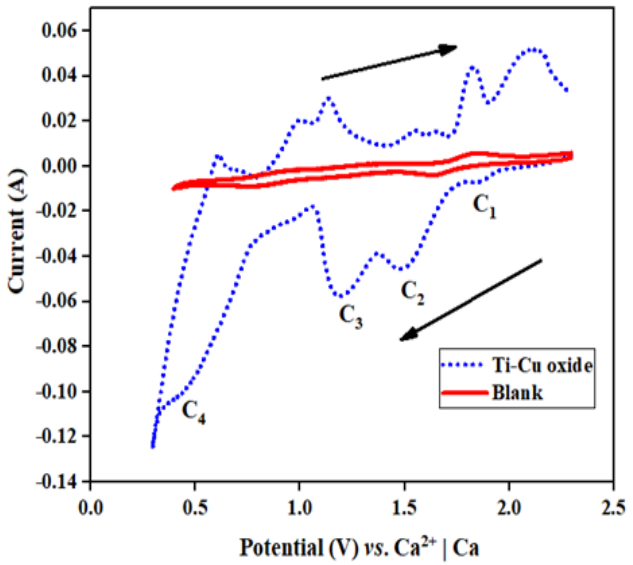


Figure 2. Cyclic voltammograms of Metallic Cavity Electrode (MCE made from Mo foil) with mixed oxide powder TiO_2-CuO (composition corresponding to Ti-10Cu alloy) and without oxide powder *vs.* $Ca^{2+}|Ca$ reference in $CaCl_2$ melt at 850 °C. Scan rate: 100 mVs^{-1}; Counter electrode: HD graphite rod.

Hu *et al.,* investigated the electrochemical behavior of TiO_2 (sandwiched between Mo substrate) by CV[33]. According to their findings, three reduction peaks were observed at -0.37 V, -0.52 V, and -1.23 V vs. the Mo wire pseudo-reference electrode. The peaks were assigned to the reduction of TiO_2 to Ti_3O_5, Ti_3O_5 to Ti_2O_3, and TiO to Ti, respectively. The reduction peaks of TiO_2 to Ti (C_2 to C_4) observed in the present study proceeded in the similar manner, respectively. A detailed reduction pathway was generated based on these four peaks (C_1 to C_4). The standard reduction potentials, calculated using FactSage 8.2 thermochemical database[34] (*vs* $Ca^{2+}|Ca$) listed in Table 1 and the findings from the literature mentioned above suggest that the following cathodic reactions could be involved in the reduction peaks of C_1, C_2, C_3, and C_4. It should be clarified that the thermodynamic data presented in Table 1 represent

Table 1. Standard reduction potentials of metal oxides at 850 °C vs. $Ca^{2+}|Ca$[34]

Reaction	Standard reduction potential (E^0)
$O_2 + 4e^- \rightarrow 2O^{2-}$	2.691 V
$2Cu_2O + 4e^- \rightarrow 4Cu + 2O^{2-}$ $2CuO + 4e^- \rightarrow 2Cu_2O + O^{2-}$	2.467 V 2.356 V
$6TiO_2 + 4e^- \rightarrow 2Ti_3O_5 + 2O^{2-}$	1.356 V
$4TiO_2 + 4e^- \rightarrow 2Ti_2O_3 + 2O^{2-}$	1.277 V
$2TiO_2 + 4e^- \rightarrow 2TiO + 2O^{2-}$	0.985 V
$Ti_3O_5 + 4e^- \rightarrow 3TiO + 2O^{2-}$	0.929 V
$2Ti_2O_3 + 4e^- \rightarrow 4TiO + 2O^{2-}$	0.825 V
$TiO_2 + 4e^- \rightarrow 2Ti + 2O^{2-}$	0.6465 V
$2CaTiO_3 + 4e^- \rightarrow 2TiO + 2CaO + 2O^{2-}$	0.531 V
$2/5\ Ti_3O_5 + 4e^- \rightarrow 6/5\ Ti + 2O^{2-}$	0.531 V
$2/3\ Ti_2O_3 + 4e^- \rightarrow 4/3\ Ti + 2O^{2-}$	0.442 V
$2TiO + 4e^- \rightarrow 2Ti + 2O^{2-}$	0.311 V
$2Ca^{2+}\ 4e^- \rightarrow 2Ca$	0.000 V

standard reduction potentials (E^0) extracted directly from the FactSage 8.2 thermochemical database under standard states. This analysis is distinct from real-time Gibbs free-energy minimisation or multi-component equilibrium calculations.

$Cu_2O + 2e^- \rightarrow 2Cu + O^{2-}$ C_1

$6TiO_2 + 4e^- \rightarrow 2Ti_3O_5 + 2O^{2-}$ C_2

$4Ti_3O_5 + 4e^- \rightarrow 6Ti_2O_3 + 2O^{2-}$ C_3

$2Ti_2O_3 + 4e^- \rightarrow 4TiO + 2O^{2-}$

$2TiO + 4e^- \rightarrow 2Ti + 2O^{2-}$ C_4

3.3 Constant Voltage Electrolysis of TiO_2-CuO Mixed Oxide Pellet

The theoretical decomposition potentials of TiO_2 and CuO at 850 °C calculated using FactSage 8.2 are 1.919 V and 0.290 V, respectively[34]. Constant voltage electrolysis was conducted at a voltage of 3.1 V between the TiO_2-CuO (corresponding to Ti-10Cu) mixed oxide cathode and a high-density graphite anode in a molten $CaCl_2$ electrolyte at 850 °C. The applied cell voltage of 3.1 V was adequate to reduce the individual oxides; however, it was less than the decomposition voltage of $CaCl_2$ (E^o = 3.262 V). The electrolysis was conducted over varying durations to investigate the mechanism of the electro-reduction process. The current-time response during constant voltage electrolysis at 850 °C, conducted for 0.5 h, 2 h, 5 h, 8 h, and 15 h, is shown in Figure 3.

Under the applied voltage, the cell current increased to a maximum of 2.09 A at the start of electrolysis, and gradually decreased to approximately 0.97 A, within 0.5 h (inset). As the electrolysis continued, the cell current decreased further and underwent a sequence of slopes and plateaus, eventually stabilized at 0.13 A after 15 h. This sharp initial rise in current at the onset of reduction occurs to reduce the high concentration of oxide species at the surface, as the outermost layer is most accessible to the electrolyte (molten $CaCl_2$). As the reduction proceeds inwards, the oxide concentration

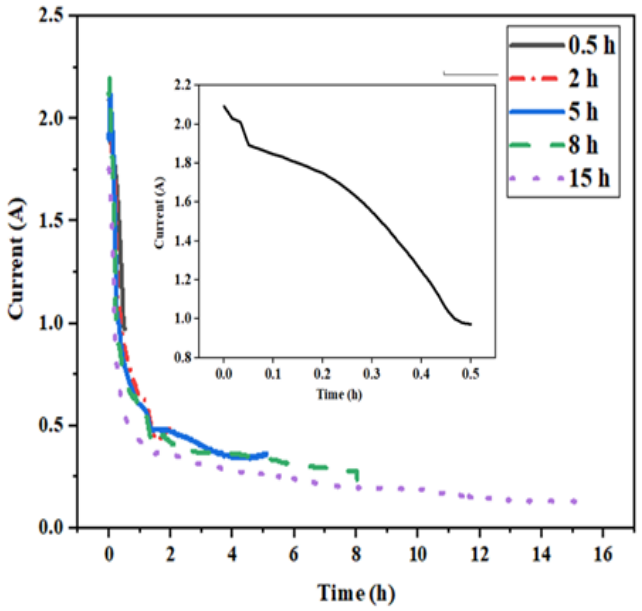


Figure 3. The variation of current with time during constant voltage electrolysis at 3.1 V for 0.5 h, 2 h, 5 h, 8 h and 15 h with sintered TiO_2-CuO oxide pellet cathode (composition corresponding to the Ti-10Cu alloy) and HD graphite anode in $CaCl_2$ melt at 850 °C. Inset shows the current variation at the onset of electrolysis.

decreases causing the current to decline or stabilize while incomplete reduction or the persistence of intermediate phases (such as Ti_2O_3 or TiO) further retards the process[35].

After the electrolysis, the cathode products were washed several times with cold water to remove any adhering salts, followed by drying under vacuum. After washing and drying, the product showed a shiny metallic texture, indicating the formation of a metal or alloy. The dried cathode products were characterized by XRD, and the phases formed during the electro-reduction process are summarized in Table 2. Powder XRD patterns of samples electrolyzed for 0.5 h – 5 h are shown in Figure 4. The phase composition of the XRD pattern for the 0.5-hour electrolyzed product includes $CaTiO_3$, $CaTi_2O_4$, Ti_2O_3 (rhombohedral), and Cu. In

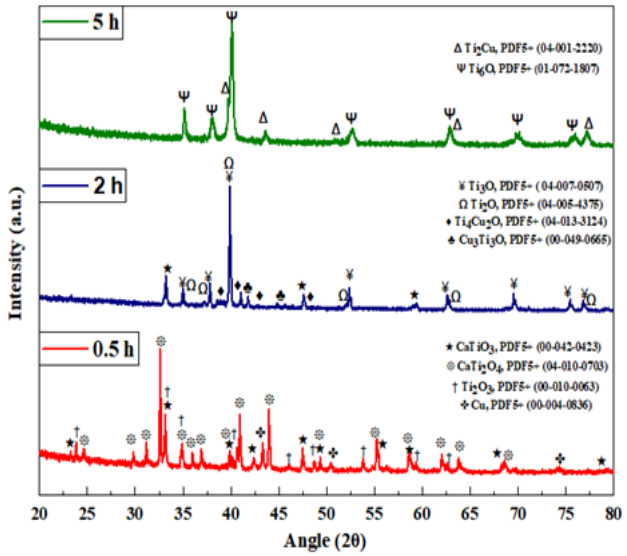


Figure 4. XRD patterns of TiO_2-CuO (corresponding to the Ti-10Cu alloy) pellets after constant voltage electrolysis experiments at 3.1 V (electro-deoxidation) conducted for 0.5 h, 2 h and 5 h.

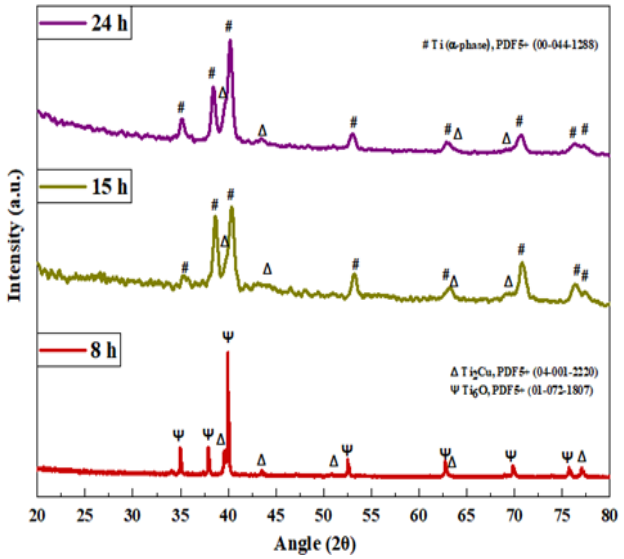


Figure 5. XRD patterns of TiO_2-CuO (corresponding to the Ti-10Cu alloy) pellets after constant voltage electrolysis experiments at 3.1 V (electro-deoxidation) conducted for 8 h, 15 h and 24 h.

the initial phase of electrolysis, maintaining a voltage of 3.1 V enabled the reduction of less stable oxide CuO to metallic Cu. Upon increasing the electrolysis time to 2 h, Ti_2O_3 was reduced to Ti_3O and Ti_2O. A small amount of intermetallic oxide phases, Ti_4Cu_2O and Ti_3Cu_3O, was detected in the XRD pattern of the 2-h electrolyzed product. The formation of ternary oxides could be due to a solid-state reaction between the oxygen-rich Ti phase and Cu above 700 °C under inert conditions, as reported in the literature[36]. Their results demonstrate that the Ti_3Cu_3O phase is thermodynamically less stable under inert conditions than the Ti_4Cu_2O phase. Consequently, as the reaction progresses, Ti_3Cu_3O readily transforms *in situ* into the more stable Ti_4Cu_2O phase. After 5 h of electrolysis, the $CaTiO_3$ phase was absent, and an ordered hexagonal Ti_6O phase appeared, along with the Ti_2Cu phase. Ti_2Cu could have formed from the reduction of Ti_4Cu_2O. These same phases persisted even after 8 hours of electrolysis. Further increasing the electrolysis time to 15 hours (Figure 5) resulted in the formation of the α-Ti phase, along with

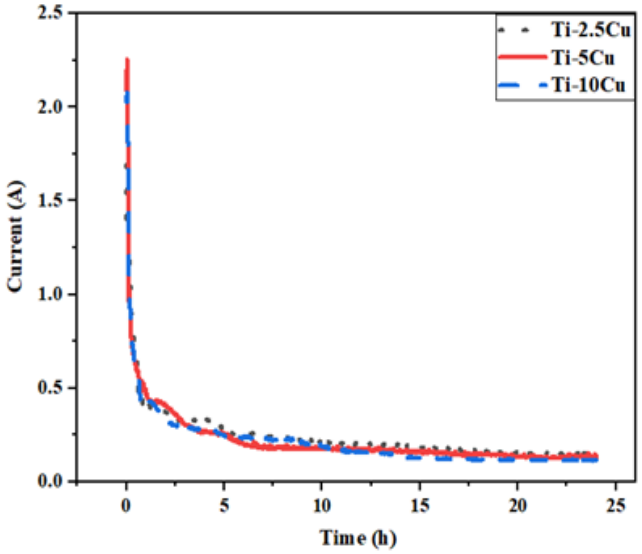


Figure 6. The variation of current with time during constant voltage electrolysis at 3.1 V (electro-deoxidation) for 24 h with sintered TiO_2-CuO mixed oxide pellets (corresponding to the alloy compositions of Ti-2.5Cu, Ti-5Cu and Ti-10Cu) and HD graphite anode in $CaCl_2$ melt at 850 °C.

the Ti_2Cu phase. XRD analysis showed that the complete metallization was achieved after approximately 15 h of electrolysis, and prolonged electrolysis (up to 24 h) was further carried out to remove some residual oxygen present in the reduced pellet. Electrolysis for the other two mixed oxides (compositions corresponding to Ti-2.5Cu and Ti-5Cu alloy) was also done for 24 h, and their respective current *vs* time plot is shown in Figure 6. All three cathode products (namely Ti-2.5Cu, Ti-5Cu and Ti-10Cu alloys) were subsequently characterized using XRD (Figure 7) (Ti-10Cu alloy XRD pattern in (Figure 5) and SEM-EDS analyses.

Table 2. XRD results (from Figures. 4 and 5) of the constant voltage electrolysis experiments conducted at 3.1V for different time durations with sintered TiO_2-CuO (corresponding to the Ti-10Cu alloy) oxide pellet in $CaCl_2$ melt at 850 °C.

Time (h)	Phases
0.5 h	$CaTi_2O_4$, $CaTiO_3$, Ti_2O_3, Cu
2 h	$CaTiO_3$, Ti_3O, Ti_2O, Ti_4Cu_2O, Ti_3Cu_3O
5 h	Ti_6O, Ti_2Cu
8 h	Ti_6O, Ti_2Cu
15 h	Ti (α), Ti_2Cu
24 h	Ti (α), Ti_2Cu

The mechanistic pathway of TiO_2 electro-reduction is well studied in the literature, especially in $CaCl_2$-based melts[37]. The reduction pathway studied by Schwandt and Fray involved several intermediate phases, including the formation and breakdown of different suboxides of Ti (namely Ti_3O_5, Ti_2O_3, and TiO) and ternary calcium titanates, such as $CaTiO_3$ and $CaTi_2O_4$. The formation of these titanates at the initial stage of the electrolysis process could also be observed. In the subsequent stages, these titanates were reduced to Ti_3O and Ti_2O, as observed in the XRD pattern of the 2 h-electrolyzed pellet. The final

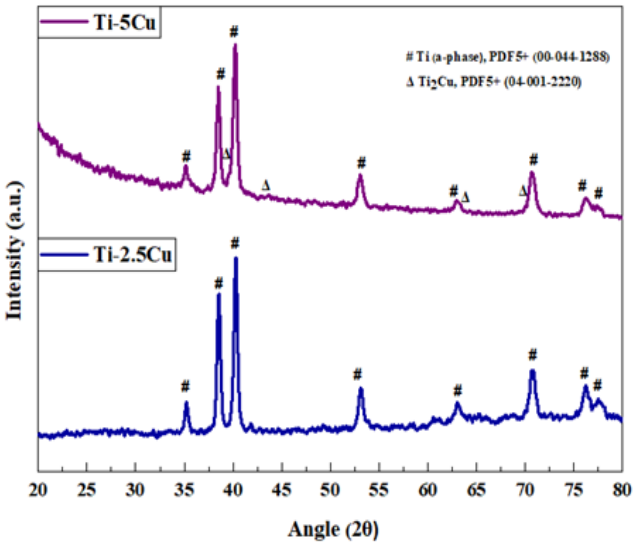


Figure 7. XRD patterns of Ti-2.5Cu alloy and Ti-5Cu alloy after electro-deoxidation conducted at 3.1 V for 24 h.

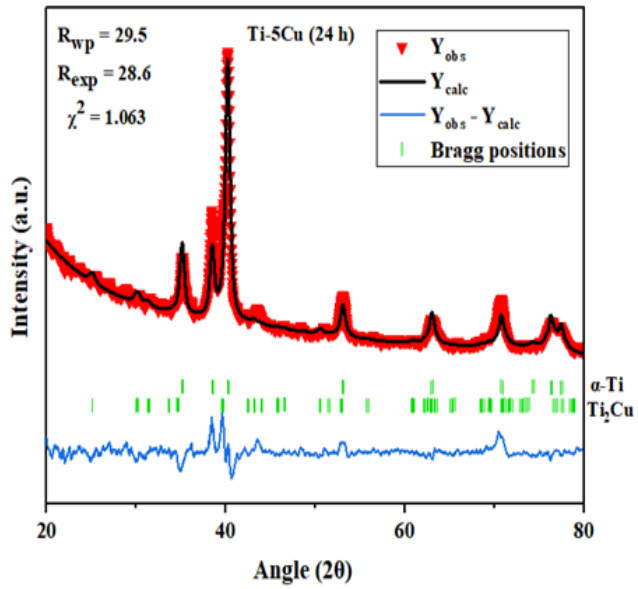


Figure 8. Powder XRD spectra and Rietveld refinement plot for Ti-5Cu alloy obtained after electro-deoxidation at 3.1 V for 24 h in $CaCl_2$ melt at 850 °C.

intermediate oxide Ti_6O is formed from the reduction of Ti_3O and Ti_2O phases, as seen in the XRD plots of 5 h and 8 h electrolyzed pellets, respectively. According to studies conducted by Khan *et al.,* it was observed that both V_2O_3 and Cr_2O_3 reduction assisted in the faster

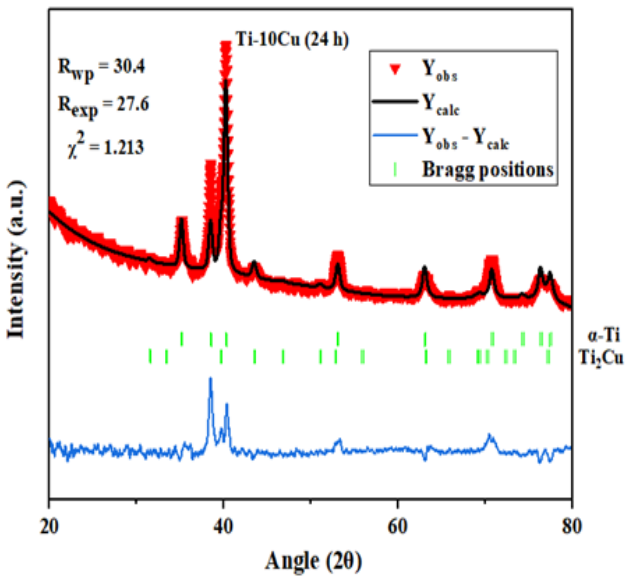


Figure 9. Powder XRD spectra and Rietveld refinement plot for Ti-5Cu alloy obtained after electro-deoxidation at 3.1 V for 24 h in $CaCl_2$ melt at 850 °C.

reduction of TiO_2[29]. In a similar manner, the reduction of Cu_2O and the formation of the Ti_2Cu phase also facilitated the reduction of TiO_2.

To quantify the phases (α-Ti and Ti_2Cu) obtained in the XRD patterns of Ti-Cu alloys (electro-reduction for 24 h), Rietveld refinement was performed using FullProf software, employing a pseudovoigt profile function along with axialdivergence corrections appropriate for the instrument geometry and divergence conditions. XRD of Ti-2.5Cu alloy showed only the α-Ti phase. Since XRD cannot reliably detect phases below 5 wt.%, the Ti_2Cu phase is not observed in the Ti-2.5Cu alloy, hence Rietveld refinement was not performed. The α-Ti phase crystallizes in hexagonal geometry with the lattice parameters of a = b = 2.95 Å, c = 4.68 Å, and α = β = 90°, γ = 120°. Ti_2Cu phase crystallizes in tetragonal geometry with a = b = 2.9438 Å, c = 10.7861 Å, and α = β = γ = 90°. The refined XRD patterns of the Ti-5Cu and Ti-10Cu alloys are shown in Figures 8 and 9. For Ti-5Cu, the reduced lattice parameters of α-Ti and Ti_2Cu obtained after Rietveld refinement were a = b = 2.939291 Å, c = 4.664837 Å and a = b = 2.829739 Å, c = 10.758913 Å, respectively. The phase composition present in Ti-5Cu was determined to be α-Ti = 92.8 wt.% and Ti_2Cu = 7.2 wt.%. In the case of Ti-10Cu, the reduced lattice parameters of α-Ti and Ti_2Cu obtained after Rietveld refinement were a = b = 2.949351 Å, c = 4.679685 Å and a = b = 2.943597 Å, c = 10.7289 Å, respectively. The phase composition present in Ti-10Cu was determined to be α-Ti = 83.5 wt.% and Ti_2Cu = 16.5 wt.%. Based on the MCE CV data and the XRD results obtained at different electrolysis intervals, a probable step-by-step electro-deoxidation pathway is proposed. Given the dynamic nature of molten salt electrolysis, these reactions (Equations 1–12) shall be interpreted as a chronological progression of dominant phases rather than a strictly isolated, sequential reaction chain.

$$2CuO + 2e^- \rightarrow Cu_2O + O^{2-} \quad [1]$$

$$Cu_2O + 2e^- \rightarrow 2Cu + O^{2-} \quad [2]$$

$$TiO_2 + Ca^{2+} + O^{2-} \rightarrow CaTiO_3 \quad [3]$$

$$2CaTiO_3 + 2e^- \rightarrow Ti_2O_3 + 2CaO + O^{2-} \quad [4]$$

$$2CaTiO_3 + Ti_2O_3 + 2e^- \rightarrow 2CaTi_2O_4 + O^{2-} \quad [5]$$

$$2CaTiO_3 + 6e^- \rightarrow Ti_2O + 2CaO + 3O^{2-} \quad [6]$$

$$3CaTi_2O_4 + 14e^- \rightarrow 2Ti_3O + 3CaO + 7O^{2-} \quad [7]$$

$$4TiO + 2Cu + 6e^- \rightarrow Ti_4Cu_2O + 3O^{2-} \quad [8]$$

$$3Ti_2O + 2e^- \rightarrow 2Ti_3O + O^{2-} \quad [9]$$

$$2Ti_3O + 2e^- \rightarrow Ti_6O + O^{2-} \quad [10]$$

$$Ti_4Cu_2O + 2e^- \rightarrow 2Ti_2Cu + O^{2-} \quad [11]$$

$$Ti_6O + 2e^- \rightarrow 6Ti + O^{2-} \quad [12]$$

3.4 Microstructural Characterization of the Alloys

The morphological changes that occurred before and after electro-reduction were examined using SEM-EDS for both mixed oxide precursors and the reduced alloys. SEM images of the Ti-2.5Cu electrolyzed

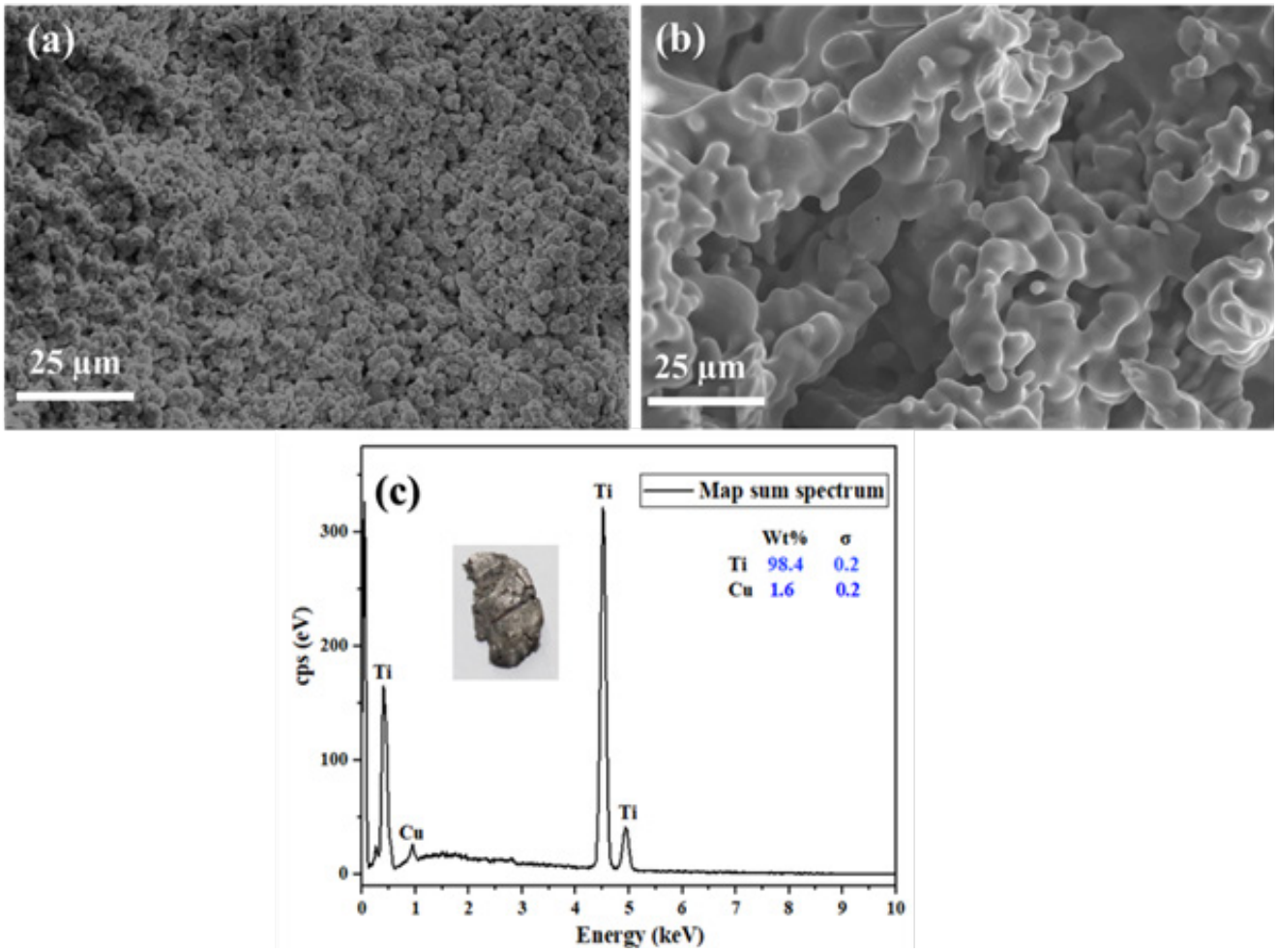


Figure 10. SEM images (1000X magnification) of the cross-sections of **(a)** TiO_2-CuO mixed oxide pellet, sintered at 900 °C in air for 4 h, corresponding to the Ti-2.5Cu alloy composition, **(b)** Ti-2.5Cu alloy (24 h electrolyzed product) and **(c)** EDS map sum spectrum (inset shows the electro-reduced Ti-2.5Cu alloy).

product (Figure 10) revealed that the smaller particles present in the mixed oxide matrix transformed into a porous interconnected nodular structure, indicating the onset of phase transformation and alloy formation. It is evident that the oxides were converted into alloys with larger particle sizes and distinct, comparatively homogeneous microstructures. This change in particle size depends on the reduction kinetics and precursor morphology. The Ti_2Cu phase could not be observed for the Ti-2.5Cu alloy, as evident from its XRD pattern; therefore, the morphology was similar to that obtained for pure Ti by the electro-reduction process[38]. The absence of the Ti_2Cu phase may be due to the conventional detection limits of laboratory X-ray diffraction. The phase may exist as ultra-fine or low-volume fraction precipitates dispersed within the matrix.

According to the Ti-Cu binary phase diagram, the β-Ti phase undergoes eutectoid decomposition into the α-Ti and Ti_2Cu phases at temperatures ranging from 790 to 850 °C, depending on composition and cooling rate. The eutectoid reaction of β-Ti → α-Ti + Ti_2Cu was observed in the case of Ti-5Cu, forming a two-phase, interconnected, nodular morphology with an irregularly precipitated Ti_2Cu phase across the α-Ti phase (Figure 11 (a)). The precipitated

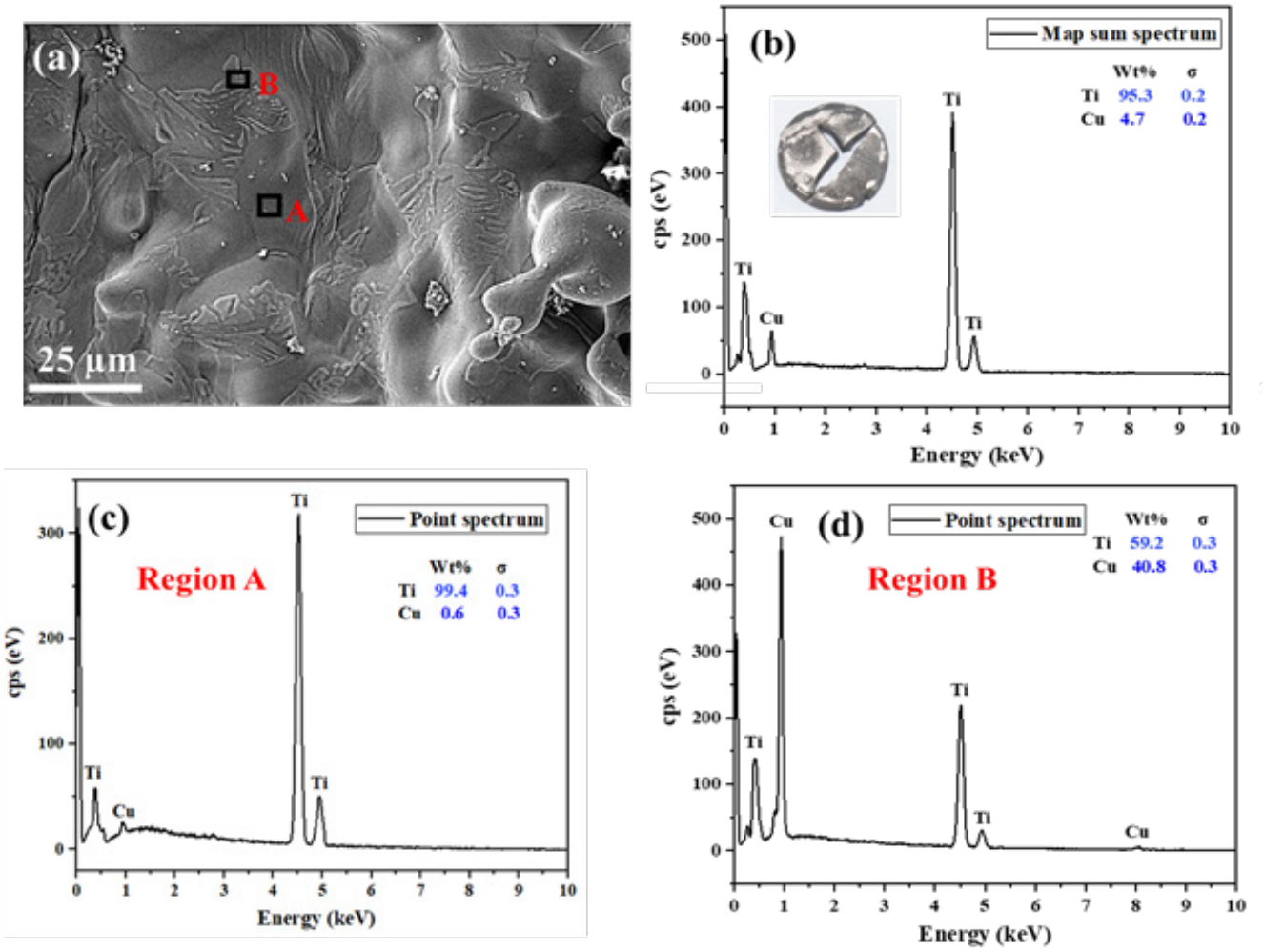


Figure 11. **(a)** SEM image (1000X magnification) of the cross-section of Ti-5Cu alloy, **(b)** map sum spectrum of Ti-5Cu, **(c)** & **(d)** EDS spectrum taken from regions A and B shown in (a) (α-Ti and Ti_2Cu phase).

Ti_2Cu phase was clearly confirmed by the EDS point spectrum obtained from region B (Figure 11 (d)). The composition of the obtained elements nearly matched the theoretical values for Ti (60.12 wt.%) and Cu (39.88 wt.%). The major α-Ti phase could also be confirmed from the EDS point spectrum obtained from region A (Figure 11 (c)).

Figures 12 (a) – 12 (c) show the cross-sectional SEM image and the elemental mapping of Ti and Cu of the Ti-10Cu alloy. The SEM image shows that the Ti_2Cu phase got dispersed within the matrix of the α-Ti phase as a result of the hyper-eutectoid reaction[14]. By comparing the SEM morphologies of the three alloys, it was observed that variations in Cu content resulted in different microstructural changes in the Ti-Cu alloys. In the Ti-5Cu alloy, Ti_2Cu morphology can be seen in the form of irregular precipitates, while in the Ti-10Cu alloy, this phase is completely dispersed into the α-Ti matrix (inset). An increased copper content enhances the growth of Ti_2Cu precipitates during solidification, promoting the elongated embedding of these precipitates within the α-Ti matrix. Thus, the morphology of the Ti_2Cu phase changes from irregular precipitates in the Ti-5Cu alloy to completely dispersed in the Ti-10Cu alloy[39].

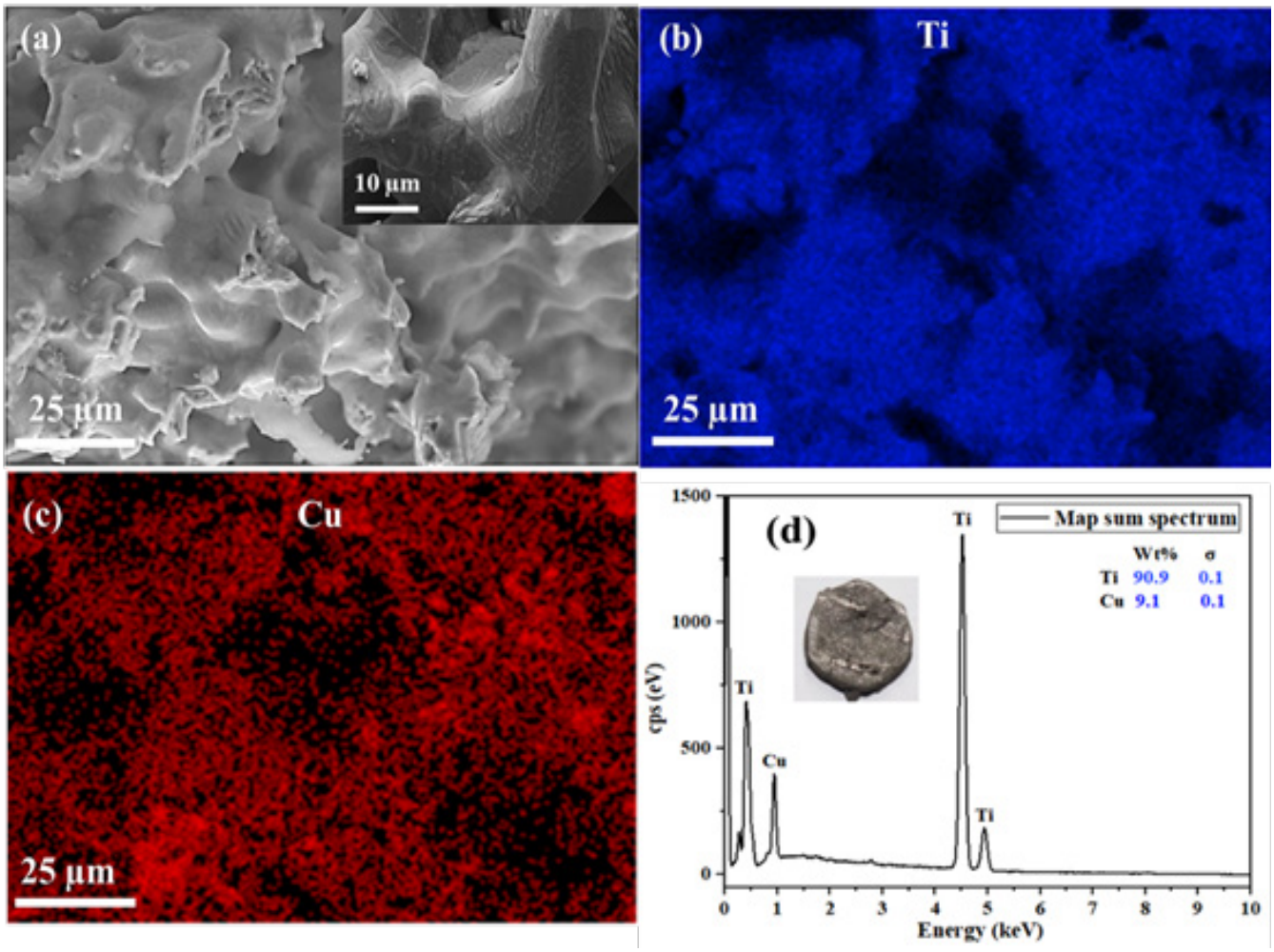


Figure 12. **(a)** SEM cross-sectional image of Ti-10Cu alloy (24 h electrolyzed product) (inset shows the SEM image of the same in 3000X magnification) **(b)** and **(c)** EDS elemental mapping of Ti and Cu across the reduced product (cross-section) and **(d)** EDS map sum spectrum (inset shows the reduced Ti-10Cu); Magnification: 1000X.

EDS map sum spectra of the cross-section of all the alloys confirmed the presence of only Ti and Cu in the alloy, with no detectable contamination from other elements such as Ca, Cl and O. EDS map-sum spectra (area scan) conducted across the cross-sections of the Ti–2.5Cu, Ti–5Cu, and Ti–10Cu alloys yielded measured copper concentrations of 1.6 wt.% [Figure 10 (c)], 4.7 wt.% [Figure 11 (b)] and 9.1 wt.% (Figure 12 (d)) respectively. These values are in near agreement with the nominal compositions. ICP-OES analysis of the products obtained after 24 h of electrolysis revealed the following compositions: Ti–5Cu alloy contained 93.8 (±4.69) wt.% Ti and 3.7 (±0.185) wt.% Cu, while Ti–10Cu alloy exhibited 91.7 (± 4.585) wt.% Ti and 8.7 (± 0.435) wt.% Cu. The oxygen content in the electro-reduced Ti-Cu alloys was determined using an elemental analyzer and was found to be 200-250 ppm.

3.5 Mechanical Properties of the Alloys

The mechanical properties of Ti-Cu alloys are largely governed by factors such as Cu content, fabrication techniques, and post-treatment procedures[40]. Alongside these factors, the compositional uniformity

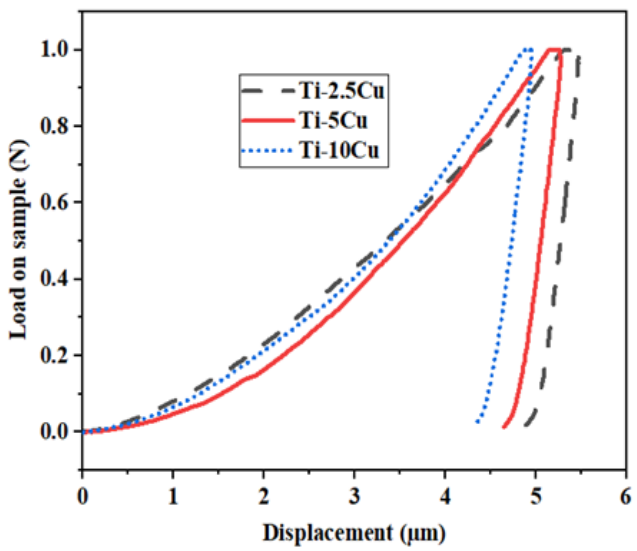


Figure 13. Force *vs* displacement curves of 4-point bending tests of Ti-Cu alloys in the as-prepared state.

and microstructural control can directly govern the strength and hardness[41]. Figure 13 shows the force-displacement curves for the alloy in its as-prepared form. Up to the breakdown point, each alloy responded linearly. Table 3 summarizes the mechanical parameters of the Ti-Cu alloys.

The elastic modulus is controlled by a complex interaction of factors, including chemical composition, phase fraction, porosity and microstructural features such as grain size and texture[42]. In Ti–Cu alloys, the elastic modulus increases as copper content increases, owing to a greater fraction of stiff intermetallic phase (Ti_2Cu), which is much more rigid than the α-Ti matrix and enhanced Cu solid-solution strengthening[42,43]. Highly porous alloys (>40%) exhibit elastic moduli below 30 GPa due to reduced load-bearing area and stress-concentration effects from interconnected pores, thereby rendering the metallic framework a scaffold-like structure with reduced stiffness. Hence, highly porous Ti-Cu alloys are significantly advantageous in biomedical applications[44]. In this study, the elastic moduli of Ti–2.5Cu, Ti–5Cu, and Ti–10Cu alloys were determined to be 62.8, 80.5, and 91 GPa, respectively, corresponding to open porosity values of 22.44%, 21.63%, and 20.47%. Thus, as porosity decreased, the elastic modulus increased, as reported for porous alloys[45,46]. By applying a constant load of 1 N in all three alloys, the differences in displacement become evident. Ti-10Cu has the highest elastic modulus among them since it shows the least displacement.

Because of the presence of controlled open porosity (around 20-22%), polished cross-sections of the alloy samples were used for Vickers hardness measurements. Several measurements (5-7) were carried out for each Ti-Cu alloy sample, and the corresponding average Vickers hardness values are presented in Table 3,

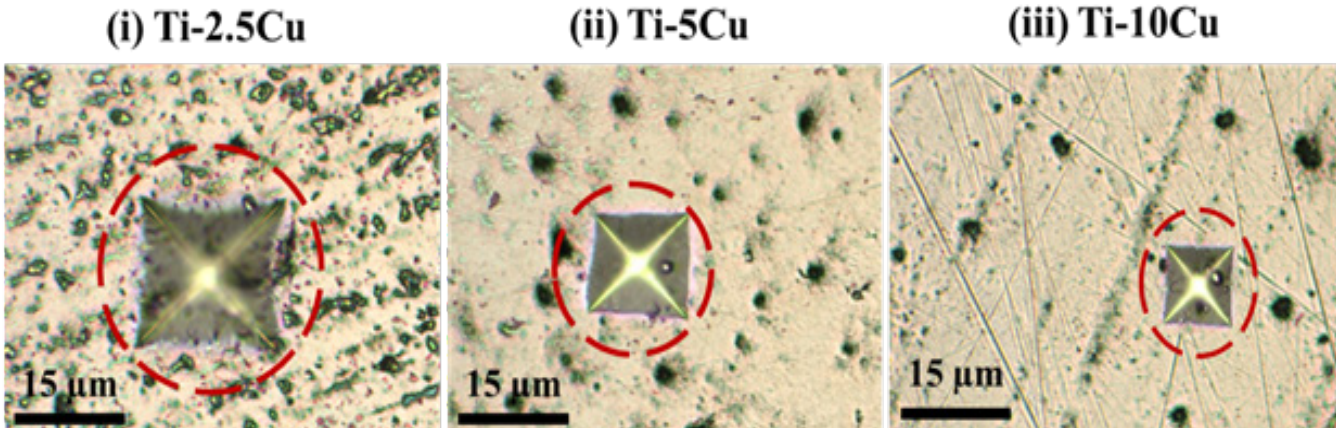


Figure 14. Optical micrographs of Vickers indentations on the as-prepared state of Ti-Cu alloys.

Table 3. Elastic modulus and hardness values of the as-prepared Ti-Cu alloys

Alloy	Elastic modulus (GPa)	Average Vickers Hardness (HV) (Coefficient of variation)
Ti-2.5Cu	62.8	90.71 (11.89%)
Ti-5Cu	80.5	159.6 (8.9%)
Ti-10Cu	91	170 (7.31%)

along with the coefficients of variation. As the Cu content increases, the hardness of the Ti-Cu alloy also rises, as indicated in Table 3. It may be due to the precipitation of the Ti_2Cu phase and the solid-solution hardening of α-Ti[47]. The enhancement of solution strengthening and grain refinement is limited when the Cu content exceeds 5 wt.%, as evidenced by the hardness value of the Ti-10Cu alloy (170 HV), which is approximately 10 HV higher than that of the Ti-5Cu alloy (159.6 HV). Light optical images of the Vickers indentations produced during the hardness tests are shown in Figure 14. The pictures demonstrate that the indentations were captured on the alloy's minimally porous regions and were free of corner and edge cracks. An increase in indentation size is observed in the Ti-2.5Cu alloy compared to the other two alloys, which may be attributed to the inverse relationship between indentation size and Vickers hardness[48]. The gradual change in the indent shape suggests a shift from ductile to semi-ductile behavior in Ti-Cu alloys as the copper content increases.

3.6 Corrosion Behavior of the Alloys

Figure 15 shows the potentiodynamic polarization curves of Ti, Ti-2.5Cu, Ti-5Cu, and Ti-10Cu alloys after 24 h of immersion in 3.5 wt.% NaCl solution. The NaCl solution (3.5 wt.%) is used to replicate the chloride-rich marine environment in which Ti alloy structural components are used[49]. In electrochemical corrosion testing, the corrosion potential (E_{corr}) reflects the thermodynamic tendency for material to corrode, i.e., its susceptibility, while the corrosion current density (I_{corr}) quantifies the kinetics, representing how quickly corrosion proceeds under given conditions[43]. In

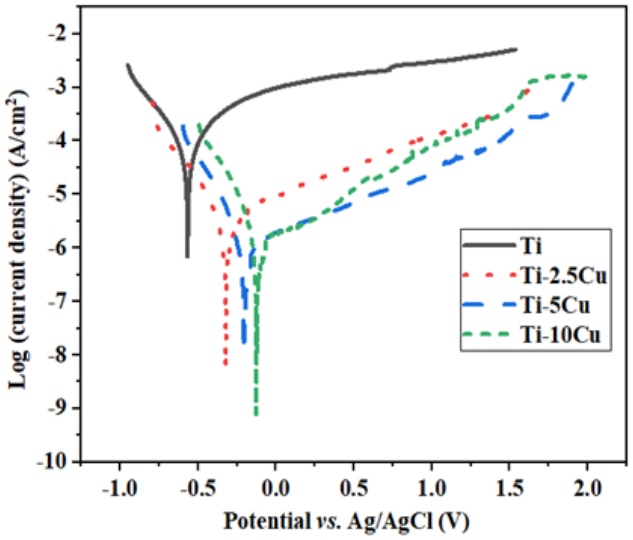


Figure 15. Potentiodynamic polarization curves of Ti and Ti-Cu alloys immersed in 3.5 wt.% NaCl solution for 24 h.

Table 4. Corrosion parameters of the alloys prepared, as obtained from potentiodynamic polarization curves

Alloy	E_{corr} (V)	I_{corr} ($\mu A/cm^2$)	*Rp* ($k\Omega.cm^2$)
Ti	-0.56	35.9	0.73
Ti-2.5Cu	-0.322	1.12	23.25
Ti-5Cu	-0.206	0.496	52.58
Ti-10Cu	-0.128	0.685	38.07

general, the better corrosion resistance of the material is indicated by a less negative or more positive E_{corr} and a lower I_{corr}.

The corrosion parameters for all the alloys, obtained from their respective polarization plots, are listed in Table 4. A broad passivation region spanning from around +0.5 to about +1.5 V versus Ag/AgCl was observed for all alloys. The corrosion current density and the corrosion potential of the prepared Ti-Cu alloys were comparatively low when compared to the pure Ti prepared under the same experimental conditions. The E_{corr} values became more positive as the Cu content increased from 2.5 wt.% to 10 wt.% in Ti-Cu alloys, indicating the formation of protective passivation layers. However, the lowest I_{corr} was observed for the Ti-5Cu alloy. The polarization resistance (R_p) values were much higher for Ti-Cu alloys than for Ti, owing to the formation and strengthening of the protective

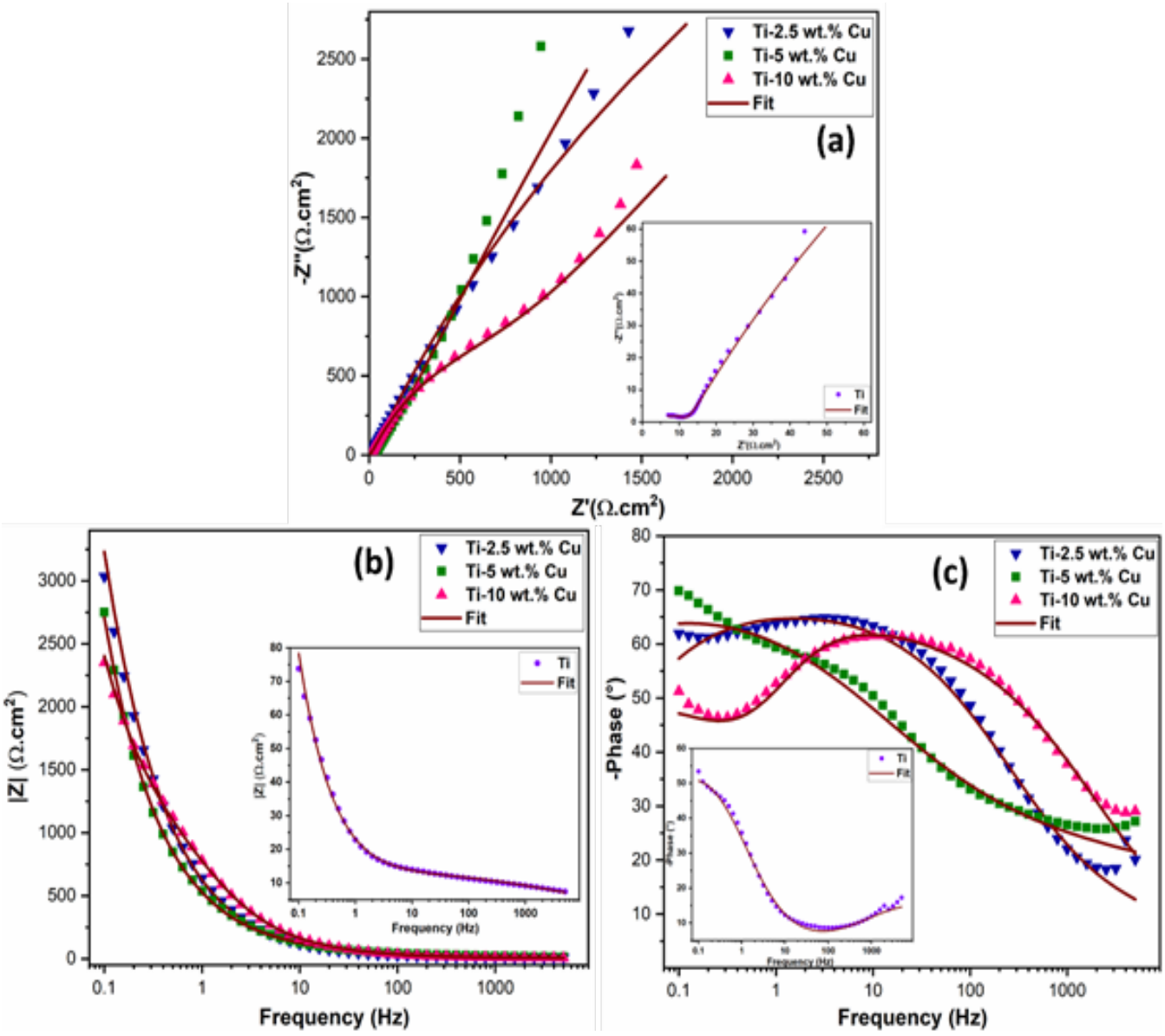


Figure 16. **(a)** Nyquist, **(b)** Bode, and **(c)** Bode phase angle plots and corresponding equivalent circuit fits for Ti and Ti-Cu alloys immersed in 3.5 wt.% NaCl solution for 24 h.

oxide film on the alloy surface[50]; the highest Rp was recorded for the Ti-5Cu alloy.

EIS measurements were also carried out at open-circuit potentials with Ti and the Ti-Cu alloys after immersing in 3.5 wt.% NaCl solution for 24 h. Figure 16 (a-c) depicts the recorded Nyquist, Bode, and Bode phase angle plots. Flattened capacitive semi-circles were observed in the Nyquist plots (Figure 16 (a)), which might indicate the combined effects of charge-transfer resistance and double-layer capacitance[26,51]. The absolute impedance was found to increase linearly with decreasing frequency, and the maximum phase angle recorded was 60-70° (Figure 16 (b and c)), indicating a capacitive signature. The passivation bilayer on Ti-Cu alloys has been reported in the literature[26,51,52]; hence, the equivalent circuit used to fit the complex impedance data was ($R_s(CPE_1R_1)(CPE_2R_2)$). Table 5 presents the values of the various circuit elements obtained from the fit. It can be observed that the solution resistance (R_s) for all the samples remained constant. Higher charge-transfer resistance (R_1 and R_2) was observed in Ti-Cu alloys than in Ti, with the highest charge-transfer resistance recorded for the Ti-5Cu alloy.

The results of the linear polarization and EIS studies indicated that the Ti-5Cu alloy is expected to exhibit the most effective corrosion resistance, as evidenced by the more positive E_{corr} and lowest I_{corr} values, the highest R_p and charge transfer resistance values. Wang *et al.* reported that a much higher concentration of the Ti_2Cu phase in the α-Ti matrix can degrade the corrosion resistance of Ti-Cu alloys by increasing micro-galvanic corrosion, thereby accelerating α-Ti corrosion, resulting in better corrosion resistance in Ti-4Cu than in Ti-10Cu[20]. The corrosion resistance of Ti-2.5Cu was found to be lower than that of Ti-5Cu and Ti-10Cu alloys, since the Ti_2Cu phase is either least observed or not present. These findings are consistent with the literature, indicating that the presence of a small amount of Ti_2Cu in the α-Ti matrix improves corrosion resistance[20,53,54]. However, the corrosion resistance of Ti-Cu alloys still remains a subject of debate, with conflicting results reported in the literature[19,55]. The processing techniques, subsequent heat treatment, and the resulting Ti_2Cu phase distribution together determine the corrosion resistance of Ti-Cu alloys[20,52]. Additionally, the porosity of the alloys plays a significant role in determining corrosion resistance. A study

Table 5. Values of the equivalent circuit elements for the fits of the EIS data recorded for Ti and Ti-Cu alloys immersed in 3.5 wt.% NaCl solution for 24 h.

(CPE = Constant phase element)

Alloy	R_s Ω.cm²	R_1 (kΩ.cm²)	CPE_1		R_2 (kΩ.cm²)	CPE_2		χ^2
			Y_0 (Ω.cm²)	n		Y_0 ($\Omega^{-1}.s^n.cm^{-2}$)	n	
Ti	3.12	0.687	0.019	0.71	0.009	0.0012	0.47	0.036
Ti-2.5 Cu	3.23	16.85	4.02 X 10^{-4}	0.75	0.032	0.042	0.15	0.12
Ti-5 Cu	2.97	54.368	5.34 X 10^{-4}	0.76	0.297	0.0046	0.29	0.09
Ti-10 Cu	3.99	42.24	6.28 X 10^{-4}	0.64	0.449	0.00045	0.92	0.068

demonstrated that the porous Ti-3Cu alloy sintered at a higher temperature (above 800 °C) exhibited better corrosion resistance in a chloride medium, with a porosity of 21.08%[46]. The Ti-xCu (x = 2.5, 5, and 10) alloys prepared in the present work exhibited porosity ranging from 20.5% to 22.4%.

4. Conclusions

In the present study, Ti-xCu (x = 2.5, 5, and 10 wt.%) alloys have been conveniently synthesized from TiO_2-CuO mixed oxide pellets via direct oxide electroreduction in molten $CaCl_2$ at 850 °C. XRD results confirmed that the crystallographic phases of the alloys depended on their Cu content, with the formation of α-Ti and Ti_2Cu phases. The electrochemical reduction behavior of a mixed oxide powder was studied using cyclic voltammetry with a metallic cavity electrode. Based on MCE CV and XRD results obtained at different time points, a probable reduction mechanism was proposed for the formation of Ti-Cu alloys. The electrochemical reduction mechanism was observed to proceed through various intermediates, including Ti_2O_3, $CaTiO_3$, Ti_2O, Ti_4Cu_2O, and Ti_6O. The complete metallization of the sintered mixed oxide pellet occurred after 15 h of electrolysis, as confirmed by XRD and SEM-EDS analyses. SEM morphological studies and EDS spectra of all the alloys clearly conveyed the distribution of both phases.

The study of mechanical properties showed that the elastic moduli and Vickers hardness values increased with increasing Cu content, with Ti-10Cu displaying the highest elastic modulus and Vickers hardness. The potentiodynamic polarization and EIS studies demonstrated improved corrosion resistance with the addition of Cu, with the Ti-5Cu alloy exhibiting the best anti-corrosion properties in 3.5 wt.% NaCl solution after 24 h immersion.

5. Acknowledgements

The authors sincerely thank Dr. Hrudanenda Jena and Dr. Ashish Jain for the XRD analysis of the samples. The authors also wish to thank Dr. Manish Chandra for SEM-EDS analysis.

6. Declaration of Competing Interest

The authors affirm that they have no financial or personal relationships that could have inappropriately influenced the research presented in this manuscript.

7. References

1. Babaremu KO, Jen TC, Oladijo PO, Akinlabi ET. Mechanical, corrosion resistance properties and various applications of titanium and its alloys: A review. J Compos Mater. 2022; 32:11. https://doi.org/10.18280/rcma.320102
2. Omran AN, Ali MM, Kh MM. Biocompatibility, corrosion, and wear resistance of β titanium alloys for biomedical applications. Appl Phys A. 2020; 126-942 https://doi.org/10.1007/s00339-020-04118-9
3. Sandu AV, Achitei DC, Perju MC, Burduhos-Nergis DD. Perspective Chapter: Titanium-A Versatile Metal in Modern Applications. Titanium-Based Alloys-Characteristics and Applications: Characteristics and Applications; 2024.
4. Yang ZG, Gong Y, Yuan JZ. Failure analysis of leakage on titanium tubes within heat exchangers in a nuclear power plant. Part I: Electrochemical corrosion, Mater Corros. 2012; 63(1);7. https://doi.org/10.1002/maco.201106189
5. Shalaby HM, Al-Mazeedi H, Gopal H, Tanoli N. Failure of titanium condenser tube. Eng Fail Anal. 2011; 18(8). https://doi.org/10.1016/j.engfailanal.2011.05.008
6. Yang XL, Du XF, Xu ZL, Liang ZS, Xiong LL. Progress in processing of porous titanium: a review. Rare Met. 2024; 43:1932. https://doi.org/10.1007/s12598-023-02570-z
7. Wang CP, Wang HZ, Ruan GL, Wang SH, Xiao XY, Jiang LD. Applications and prospects of titanium and its alloys in seawater desalination industry. Mater Sci. Eng. 2019; 688(3):033036. https://doi.org/10.1088/1757-899X/688/3/033036
8. Grass G, Rensing C, Solioz M. Metallic copper as an antimicrobial surface. Appl Environ Microbiol. 2011; 77(5):1541-1547. https://doi.org/10.1128/AEM.02766-10 PMid:21193661 PMCid:PMC3067274.

9. Jiang Y, Zhang WJ, Mi XJ, Huang GJ, Xie HF, Feng X, Peng LJ, Yang Z. Antibacterial property, corrosion and discoloration resistance of pure copper containing Zn or Ni. Rare Met. 2022; 41:4041. https://doi.org/10.1007/s12598-022-02098-8 PMid:36157376 PMCid:PMC9483388.

10. Campo KN, De Lima DD, Lopes ESN, Caram R. On the selection of Ti-Cu alloys for thixoforming processes: Phase diagram and microstructural evaluation. J Mater Sci. 2015; 50:8007. https://doi.org/10.1007/s10853-015-9367-4

11. Murray JL. The Cu-Ti (Copper-Titanium) System, Bull. Alloy Phase Diagr. 1983; 4:81. https://doi.org/10.1007/BF02880329

12. Zhang J, Cao S, Liu Y, Bao MM, Ren J, Li SY, Zhang EL, Wang JJ. Tribocorrosion behavior of antibacterial Ti-Cu sintered alloys in simulated biological environments. Rare Met. 2022; 41:1921. https://doi.org/10.1007/s12598-021-01943-6

13. Xu Y, Jiang J, Yang Z, Zhao Q, Chen Y, Zhao Y. The effect of copper content on the mechanical and tribological properties of hypo-, hyper-and eutectoid Ti-Cu alloys. Materials. 2020; 13:3411. https://doi.org/10.3390/ma13153411. PMid:32756320 PMCid:PMC7435961.

14. Luo L, Zhong Q, Chen Z, Wu X, Li S, Xue Z, Lu Y, Luo K, Zhao W. 3D-printed copper-containing tailored titanium alloys with corrosion resistance, biocompatibility and anti-inflammatory properties for enhanced guided bone regeneration, Front Bioeng Biotechnol. 2025; 13:1647678. https://doi.org/10.3389/fbioe.2025.1647678 PMid:40918437 PMCid:PMC12408666.

15. Akbarpour M, Reza M, Mirabad HM, Hemmati A, Kim HS. Processing and microstructure of Ti-Cu binary alloys: A comprehensive review. Prog Mater Sci. 2022; 127:100933. https://doi.org/10.1016/j.pmatsci.2022.100933

16. Su C, Wang Y, Wu W, Konovalov S, Huang L, Chen X. Qin S, In Situ Wire + Powder Synchronous Arc Additive Manufacturing of Ti-Cu Alloys, 3D Print. Addit Manuf. 2024; 11:163. https://doi.org/10.1089/3dp.2022.0378 PMid:38389666 PMCid:PMC10880637.

17. Zeer GM, Gordeev YI, Zelenkova EG, Abkaryan AK,Gerasimov EV, Kuchinskii MY, Zharkov SM. Effect of the Addition of Cu and Al on the Microstructure, Phase Composition and Properties of a Ti-6Al-4V Alloy Obtained by Selective Laser Melting. Metals. 2024; 14(9):2075-4701. https://doi.org/10.3390/met14090991.

18. Ohkubo C, Shimura I, Aoki T, Hanatani S, Hosoi T, Hattori M, Oda Y, Okabe T. Wear resistance of experimental Ti-Cu alloys. Biomater.2003; 24:3377. https://doi.org/10.1016/S0142-9612(03)00157-1 PMid:12809765.

19. Arkusz K, Pasik K, Nowak M, Jurczyk M. Structural, electrical and corrosion properties of bulk Ti-Cu alloys produced by mechanical alloying and powder metallurgy. Materials. 2024; 17:1473. https://doi.org/10.3390/ma17071473 PMid:38611987 PMCid:PMC11012745.

20. Wang Z, Fu B, Wang Y, Dong T, Li J, Li G, Zhao X, Liu J, Zhang G. Effect of Cu content on the precipitation behaviors, mechanical and corrosion properties of as-cast Ti-Cu alloys. Materials. 2022; 15:1696. https://doi.org/10.3390/ma15051696 PMid:35268932 PMCid:PMC8911372.

21. Chen GZ, Fray DJ, Farthing TW. Direct electrochemical reduction of titanium dioxide to titanium in molten calcium chloride. Nature. 2000; 407:361. https://doi.org/10.1038/35030069 PMid:11014188.

22. Hu D, Dolganov A, Ma M, Bhattacharya B, Bishop MT, Chen GZ, Development of the Fray-Farthing-Chen Cambridge process: towards the sustainable production of titanium and its alloys. JOM. 2018; 70:129. https://doi.org/10.1007/s11837-017-2664-4 PMid:31997875 PMCid:PMC6956875.

23. Schwandt C, Alexander DTL, Fray DJ. The electro-deoxidation of porous titanium dioxide precursors in molten calcium chloride under cathodic potential control. Electrochim Acta. 2009; 54(14):3819-3829. https://doi.org/10.1016/j.electacta.2009.02.006

24. Vishnu DSM, Sure J, Liu Y, Kumar RV Schwandt C. Electrochemical synthesis of porous Ti-Nb alloys for biomedical applications. Mater Sci Eng C. 2019; 96:466. https://doi.org/10.1016/j.msec.2018.11.025 PMid:30606556.

25. Vishnu DSM, Sure J, Kumar RV, Schwandt C. Phase composition, microstructure, corrosion resistance and mechanical properties of molten salt electrochemically synthesised Ti-Nb-Sn biomedical alloys. Mater Trans. 2019; 60:422. https://doi.org/10.2320/matertrans.MA201810

26. Liu DP, Zhang JP, Xu JL, Qi MH, Huang J, Ma YC, Luo JM. Microstructure, mechanical properties, and

corrosion resistance of Ti-Cu alloys prepared by electroless copper plating and hot-pressing sintering. J Mater Eng Perform. 2025; 1.

27. Mukherjee A, Khan MS, Kumaresan R. Studies on preparation of thorium-based intermetallics in $CaCl_2$ melt by electrochemical de-oxidation process. J Electrochem Soc. 2023; 170:102505. https://doi.org/10.1149/1945-7111/ad02c2
28. Khan MS, Mukherjee A, Kumaresan R. Preparation of U-Nb alloy from oxide precursors by direct oxide electrochemical reduction method. J Electrochem Soc. 2022; 169(6):062503. https://doi.org/10.1149/1945-7111/ac72cb
29. Khan MS, Mukherjee A, Ghosh P, Kumaresan R. Electrochemical preparation of Ti_2CrV alloy in $CaCl_2$ melt. J Electrochem Soc. 2024; 171(7):072505. https://doi.org/10.1149/1945-7111/ad6482
30. Mukherjee A, Kumaresan R, Joseph K. Studies on direct electrochemical De-oxidation of solid ThO_2 in calcium chloride-based melts. J Electrochem Soc. 2021; 168:072502. https://doi.org/10.1149/1945-7111/ac0ec8
31. Scarlat O, Zaharescu M. Thermal studies in $CuO–Cu_2O–SnO_2$ system at two oxygen pressures, as observed by DTA/TG experiments. J Therm Anal Calorim. 2002; 68(3):851-860. https://doi.org/10.1023/A:1016174018820
32. Stadt MG, Larisegger S, Nelhiebel M, Fafilek G. Identification of electrochemically formed metal oxides by coupling high-temperature cyclic voltammetry with Raman spectroscopy. J Electroanal Chem. 2024; 965:118373. https://doi.org/10.1016/j.jelechem.2024.118373
33. Hu D, Xiao W, Chen GZ. Near-net-shape production of hollow titanium alloy components via electrochemical reduction of metal oxide precursors in molten salts. Metall Mater Trans B. 2013; 14:272. https://doi.org/10.1007/s11663-013-9800-5
34. Bale CW *et al.* Reprint of: FactSage thermochemical software and databases. 2010-2016; 55:1-9. https://doi.org/10.1016/j.calphad.2016.07.004
35. Osarinmwian C, Roberts EPL. Modelling diffusion controlled electro-deoxidation of metal oxide to metal in molten salt. J Solid state electrochem. 2023; 27:3383. https://doi.org/10.1007/s10008-023-05624-5
36. Kelkar PG, Carim AH. Synthesis, properties, and ternary phase stability of M6X compounds in the Ti—Cu—O system. J Am Ceram Soc. 1993; 76:1815. https://doi.org/10.1111/j.1151-2916.1993.tb06652.x
37. Schwandt C, Fray DJ. Determination of the kinetic pathway in the electrochemical reduction of titanium dioxide in molten calcium chloride, Electrochim. Acta. 2005; 51:66. https://doi.org/10.1016/j.electacta.2005.03.048
38. Chen ZG, Fray DJ. A morphological study of the FFC chromium and titanium powders, Miner Process Extr Metall. 2006; 115:49. https://doi.org/10.1179/174328506X91365
39. Wang XS, Li SF, Misra RDK, Kondoh K, Kariya S, Yang YF. Achieving strong and ductile as-printed Ti-Cu alloys via tailoring eutectoid morphology. Mater Res Lett. 2025; 13(6):577-586. https://doi.org/10.1080/21663831.2025.2480728
40. Li K, Zhou S, Liu J, Yang F, Yang C. A review on the biomedical Ti-Cu alloys: Design, preparation, microstructure and properties. Met Adv. 2026; 39:47-67. https://doi.org/10.1016/j.metadv.2025.12.005
41. Wang Y, Chen S, Peng Y, Zheng X, Li D, Nie C, Gong P, Hu Z. Ming Ma. Effect of porosity on the corrosion behavior of FeCoNiMnCrx porous high-entropy alloy in 3.5 wt.% NaCl solution. Metals. 2025; 15:210. https://doi.org/10.3390/met15020210
42. Chaim R, Hefetz M. Effect of grain size on elastic modulus and hardness of nanocrystalline ZrO2-3 wt.% Y2O3 ceramic. J Mater Sci. 2004; 39:3057-3061. https://doi.org/10.1023/B:JMSC.0000025832.93840.b0
43. Liang XD, Zhang XG, Wang WQ, Liang JW, Zhao XZ, Liu MQ, Du SY, Zhang ZH. Tribological, corrosion and antibacterial behaviors of Ti-xCu alloy prepared by laser powder bed fusion. J Mater Res Technol. 2025; 35:5242. https://doi.org/10.1016/j.jmrt.2025.02.183
44. Tian JH, Hao J, Li YH, Wu XJ. Research progress on biocompatible sintered porous titanium alloys for hard tissue implants. Transac Ind Inst Met. 2025; 78:173. https://doi.org/10.1007/s12666-025-03649-0
45. Li YH, Chen N, Cui HT, Wang F. Fabrication and characterization of porous Ti-10Cu alloy for biomedical application. J Alloys Compd. 2017; 723:967. https://doi.org/10.1016/j.jallcom.2017.06.321
46. Tao SC, Xu JL, Yuan L, Luo JM, Zheng YF. Microstructure, mechanical properties and antibacterial properties of the microwave sintered porous Ti-3Cu

alloys. J Alloys Compd. 2020; 812:152142. https://doi.org/10.1016/j.jallcom.2019.152142

47. Mitsuhara M, Masuda T, Nishida M, Kunieda T, Fujii H. Precipitation behavior during aging in α phase titanium supersaturated with Cu. Metall Mater Trans A. 2016; 47(4):1544-1553. https://doi.org/10.1007/s11661-016-3344-7
48. Rahimi E, Rafsanjani-Abbasi A, Imani A, Hosseinpour S, Davoodi A. Insights into galvanic corrosion behavior of Ti-Cu dissimilar joint: effect of microstructure and volta potential. Materials. 2018; 11(10):1820. https://doi.org/10.3390/ma11101820 PMid:30257472 PMCid:PMC6213116.
49. Meng J, Li X, Guo F, Cheng W, Jia R. Influence of temperature on the galvanic corrosion behavior between Titanium alloy and 304 Stainless Steel in a simulated marine environment. Corros Mater Degrad. 2025; 6(4):50. https://doi.org/10.3390/cmd6040050
50. Sumanth A, Kancharla H, Mandal S, Mukherjee S, Mondal K. Effect of immersion time on the corrosion behaviour of X70 and X80 line pipe steels in simulated concrete pore solution. J Appl Electrochem. 2024; 54(10):2401. https://doi.org/10.1007/s10800-024-02108-w
51. Zadeh JM, Yeganeh M, Zaree SRA, Khorasanian M. Microstructure and corrosion behavior of Ti-10Cu fabricated by selective laser melting, Mater. Today Commun. 2024; 39:109103. https://doi.org/10.1016/j.mtcomm.2024.109103
52. Osório WR, Cremasco A, Andrade PN, Garcia A, Caram R. Electrochemical behavior of centrifuged cast and heat-treated Ti-Cu alloys for medical applications. Electrochim Acta. 2010; 55:759. https://doi.org/10.1016/j.electacta.2009.09.016
53. Ji H, Zhao MC, Xie B, Zhao YC, Yin D, Gao C, Shuai C, Atrens A. Corrosion and antibacterial performance of novel selective-laser-melted (SLMed) Ti-xCu biomedical alloys. J Alloys Compd. 2021; 864:158415. https://doi.org/10.1016/j.jallcom.2020.158415
54. Wang J, Zhang S, Sun Z, Wang H, Ren L, Yang K, Optimization of mechanical property, antibacterial property and corrosion resistance of Ti-Cu alloy for dental implant. J. Mater. Sci. Technol. 2019; 35(10): 2336-2344. https://doi.org/10.1016/j.jmst.2019.03.044
55. Liu J, Li F, Liu C, Wang H, Ren B, Yang K. Zhang E, Effect of Cu content on the antibacterial activity of titanium-copper sintered alloys. Mater Sci Eng C. 2014; 35: 392. https://doi.org/10.1016/j.msec.2013.11.028 PMid:24411393.

Author Contribution

Haritha Rajasekaran: Writing – review & editing, Writing – original draft, Visualization, Validation, Methodology, Investigation, Formal analysis, Data curation, Conceptualization. Anwesha Mukherjee: Writing – review and editing, Writing – original draft, Visualization, Validation, Methodology, Investigation, Formal analysis, Data curation. Swetha Muraleedharan: Writing – review and editing, Methodology, Formal analysis. S. Maharajan: Investigation, Formal analysis, Data curation. R. Kumaresan: Writing – review and editing Methodology, Investigation, Formal analysis, Supervision.